# Chapter 3

# Progress in Functional Neuroanatomy: Precise Automatic Geometric Reconstruction of Neuronal Morphology From Confocal Image Stacks

## 3.1 Summary

Dendritic architecture provides the structural substrate for myriads of input and output synapses in the brain and for the integration of presynaptic inputs. Understanding mechanisms of evolution and development of neuronal shape and its respective function are thus formidable problems in neuroscience. A fundamental prerequisite for finding answers is a precise quantitative analysis of neuronal structure *in situ* and *in vivo*. Therefore we have developed a tool set for automatic geometric reconstruction of neuronal architecture from stacks of confocal images. It provides exact midlines, diameters, surfaces, volumes and branch point locations, and allows analysis of labeled molecule distribution along neuronal surfaces as well as direct export into modelling software. We demonstrate the high accuracy of geometric reconstruction and show the analysis of putative input synapse distribution throughout entire dendritic trees from *in situ* light microscopy preparations as a possible application. The binary version of the reconstruction module is downloadable at no cost.

## 3.2 Introduction

The morphology of a neuron's dendritic tree is important for its computational characteristics (Euler and Denk, 2001; Koch and Segev, 2000; Mainen and Sejnowski, 1996; Rall et al., 1992) and for an adequate spatial distribution of thousands of input and output synapses. Dendritic arborizations receive, integrate, filter and process incoming synaptic information with complex spatio-temporal patterning to create structured information output which is transmitted to network partners. Therefore, network and brain function are strongly dependent upon neural architecture. The morphogenesis of dendritic trees is regulated by innate genetic factors, neuronal activity and external molecular cues (Libersat and Duch, 2004; McAllister, 2000; Miller and Kaplan, 2003; Wong and Ghosh, 2002) during developmental and experience-dependent plasticity (Spitzer, 2002; Wong and Wong, 2000). Furthermore, alterations in neural morphology may occur during ageing and neurodegenerative diseases (de Brabander et al., 1998; Uylings et al., 2000).
Despite striking achievements during recent years, neuroscience is still far from having a comprehensive understanding of the computational function of dendritic shape (Gabbiani et al., 2001; Hausser et al., 2000; Koch and Segev, 2000; Krichmar et al., 2002; Segev and London, 2000; Single and Borst, 1998; Stuart and Hausser, 2001) and of the mechanisms underlying maturation, refinement and ageing of dendritic shape in the manifold types and subtypes of neurons in the brain (Cline, 2001; Libersat and Duch, 2004; Scharff, 2000; Scott and Luo, 2001; Wong and Ghosh, 2002). A commonly available tool is needed to create neuronal morphology databases (van Pelt et al., 2001), and to quantitatively analyze changes in dendritic shape with high accuracy, as imaged during development or during learning *in situ*. Ideally, such a tool should provide precise 3-dimensional reconstruction to determine the neuron's length, diameter, surface, orientation and branching pattern (Libersat and Duch, 2004; Uylings and van Pelt, 2002) as well as its sites of input and output synapses. Only with these measures in hand can a thorough geometric evaluation, as well as the construction of models for computational analysis be performed.
Electron microscopy offers the highest precision of cellular morphology, but, due to the method's practical constraints, is only applicable to fixed tissue and is restricted to subvolumes of neurons. Confocal or two-photon microscopy offer excellent possibilities for monitoring the growth *in situ* and *in vivo* of fluorescent-stained neuronal structures at high resolution in 3 dimensions, while the neuron is in its natural environment.
Volume reconstructions, which provide surface and volume measures, are a commonly available method for the automatic reconstruction of neural morphology from confocal image stacks, but information about branching number, diameter and length must still be

determined. This, in principle, could be accomplished by a variety of methods developed to automatically extract midlines from binary volume definitions to build up a wire model of the neuronal tree that is equipped with diameters, i.e. a geometric reconstruction. Its precision, however, is limited by the quality of the volume reconstruction one starts with, and usually suffers from various algorithmic constraints which make manual post-processing necessary.

Due to the low accuracy and incomplete results of automatic procedures that are now available, geometric reconstructions are commonly done manually with programs such as Neurolucida (MicroBrightField, Inc.) (Glaser and Glaser, 1990) or Neurozoom (Neurome, Inc.). The accuracy of manual reconstruction however is strongly dependent on individual data interpretation to estimate midlines and diameters of dendrites. In addition, it is extremely time consuming. Automation therefore is a better way to create morphology databases that quantitatively link physiological function and genetic composition to morphology.

We have developed a complete and novel reconstruction tool set for creating precise geometric reconstructions as well as surface and volume reconstructions. The entire reconstruction process is fully automatic for confocal image stacks of well-stained dendritic trees as complex as those of cerebellar Purkinje cells. For even more complex dendritic trees, or for image stacks of inferior quality, the reconstruction procedure is semi-automatic. The user can manually define branch point hierarchy, and midlines and diameters of interconnecting segments are automatically determined to obtain a skeleton reconstruction. For surface reconstructions at single voxel precision, the skeleton reconstruction is used to extract localized intensity values for image segmentation to cope with staining gradients and intensity fading caused by bleaching or absorption. Furthermore, we present a method for assessing the concentration of labeled markers around the neuron's surface or within its cytoplasm to determine the distribution of labeled molecules along neuronal processes. Finally, an export routine is included to write compartment model description files from geometric reconstructions in Genesis and Neuron format for computational analysis.

This tool set offers completely new approaches to address the development, refinement, and function of neuronal architecture. To speed up database establishment and common use, it is equipped with a graphical editor to allow extensive interaction; it incorporates into the commercially available visualization software, Amira. The binary version of the reconstruction module is downloadable at no cost and its basic features are briefly documented (www.neurobiologie.fu-berlin.de/Evers.html). It requires Amira version 3.0 or 3.1 and is ready to install.

## 3.3 Methods

### 3.3.1 Intracellular staining, immunocytochemistry and image acquisition of multiple label specimens

Intracellular recording and staining of *Manduca* Motorneuron 5 was done as described in Duch and Mentel (2004). Special care was taken to avoid tissue shrinking (Bucher et al., 2000). A Leica TCS SP2 laser scanning microscope equipped with three different laser lines was used to acquire image stacks of tripple labeled preparations. All images were obtained in simultaneous acquisition mode, i.e. the emitted fluorescence light of synchronously excited fluorophores was divided by an acoustic-optical beam splitter to be detected by separate photomultipliers. Thus, no image misalignment occurred due to error in scan mirror positioning. Images were further processed with Amira 3.1 (TGS) and arranged into figures with Adobe Illustrator 10 (Adobe Systems Incorporated).

### 3.3.2 Correction for chromatic aberration

To correct for chromatic aberration of the optical path, a neuron was filled with biotin and double-labeled with Cy3- and Cy5- coupled streptavidin (Jackson Immunochemicals Inc.). An image stack was obtained as described above. The misalignment between images of the same structure was measured and corrected for in subsequent image stacks of identically-treated specimens (see (Wouterlood et al., 1998)).

### 3.3.3 Programming

All programming was done in C++, making use of Amira 3.1 (TGS) and OpenInventor (SGI) libraries for image data handling and visualization. The software was compiled for Microsoft Windows 2000 using Microsoft Visual Studio 6.0, IRIX 6.5 (SGI) using MIPSpro Compiler Version 7.41 and Suse Linux 9.0 using gcc3.3.1.

### 3.3.4 Reconstruction algorithms

The algorithms are described in detail in a parallel, theoretical paper (Schmitt et al., 2004). However, the basic principle of fitting reconstructions to confocal image data is briefly described in words below. The neuron's branchpoint hierarchy is set by the user. Then the interconnecting segments are automatically reconstructed as cylinders. This is realized by adapting the active contour model by Kass (1988). Thereby, the precision of the skeleton of interconnecting link segments is controlled by two criteria: first, the skeleton has to be

smooth, avoiding wiggles, which are due to imaging noise. This is enforced mathematically by equipping the segment with spring properties and calculating its reset force, a value which describes the segments smoothness (smoothness measure). Second, the centerline has to lie close to the middle of bright voxels (medialness), guaranteeing that the precise morphology of the neuron is reconstructed. This medialness is evaluated algorithmically and, in turn, consists of two components: First, voxels with relatively higher gray value should lie inside the neuron's circular cross-section, whereas relatively lower gray values should lie outside. Second, the change of staining intensity, i.e. the gradient of image intensities should be maximal at the circumference of the circular cross-section. Both criteria for medialness are dependent on the local staining distribution rather than on the absolute value of staining intensity.

Both the smoothness measure and medialness measure are evaluated for every cylinder, giving a numerical expression of reconstruction quality, called energy in the following. By iteratively evaluating the summed energy of the segment (i.e. the energy functional) and adjusting its midline and diameters to minimize its energy, the reconstructed segment is fitted to the confocal image data.

Precise surface reconstructions are obtained by initially calculating a 3-dimensional distance map of float values with the voxel resolution of the original image data, on which every voxel holds the distance to the nearest cylinder of the skeleton reconstruction. Negative values mark the inside of the structure and the zero-crossing the structure's boundary. The distance map is subsequently deformed to best fit the image intensity distribution, loosing the restriction to cylindrical cross sections. For this we deploy the geodesic active contour method (Caselles et al., 1997), which allows introducing several weighing criteria to judge reconstruction quality on a voxel by voxel basis. These criteria namely are staining intensity at every single compartment of the cylindrical reconstruction, local staining gradients, and a user-defined surface smoothness. The distance map is iteratively optimized adjusting the distance values of every voxel to maximize reconstruction quality. The distance map can be threshold-segmented to obtain a binary volume definition. Subsequent surface reconstruction can be generated, for example, by application of standard techniques (e.g. generalized marching cube algorithm), yielding a triangulated surface reconstruction.

### 3.3.5 Staining density and localization extraction

Staining density distribution along neuronal projections can be calculated in two different ways. If membrane-associated proteins are under investigation, the mean intensity of

$2^{nd}$ channel image data around every triangle of a triangulated surface reconstruction is calculated within a pre-defined distance and stored for every triangle. For correlation analysis between the skeleton's geometry and the staining localization, the skeleton is fragmented into truncated cones. Surface triangles are assigned to that cone-shaped compartment best approximating the triangle's location and are stored for every node. Thus staining distribution calculated for the surface reconstruction can be related to the neuron's geometry.
If the localization of cytoplasmatic proteins should be analyzed, the mean staining density within the volume corresponding to a cone-shaped compartment of the skeleton reconstruction is extracted. The node's volume is first confined to lie on the node's side of the planes orthogonally intersecting the straight lines to its neighbor nodes in their center point, and second, the volume's voxels must hold a negative value in the fitted distance map (described above). The density values are stored for every node.

### 3.3.6 Exporting geometry data for analysis

Data about tree geometry can be exported as an ASCII table and include the following values for every branch segment: successive endings, segments, number of branchpoints and tree length; length and mean radius of branch segment; tree distance and air distance to tree origin.
Tags can be individually assigned to skeleton nodes. This enables to define a selection of nodes for geometric analysis. If a geometric analysis is performed for selected nodes, the ASCII table will additionally include the following measures: length and mean radius of the branch segment the node is part of; the node's tree distance and air distance to tree origin; distance to next higher branchpoint; radius of the node; values stored for the node.

### 3.3.7 Importing three-dimensional reconstructions in non-proprietary format

An import and export filter for neuron morphology data in SWC-file format (Cannon et al., 1998) is included with the reconstruction module for Amira. This is a suggested format for online neuronal morphology databases, as used at http://www.cns.soton.ac.uk/~jchad/cellArchive/cellArchive.html. This file format is supported by CVAPP, a program for viewing and simple editing available from the above address, and which also supports the import of Neurolucida reconstructions. Like this, it is possible to process Neurolucida

reconstructions within Amira.

## 3.4 Results

Here we present a comprehensive new reconstruction tool-set for measuring precise geometric parameters, describing the morphology of 3-dimensional neuronal processes. The tool-set consists of 4 components.

1. A semi-automatic reconstruction procedure is realized by adapting the snake algorithm (Kass, 1988; Schmitt et al., 2004) to trace approximately tubular neuronal structures in confocal image stacks. User interaction is needed to define branch point hierarchy, whereby the algorithm automatically determines the midline and diameter of interconnecting link segments at a user-predefined step size. The resulting tubular reconstruction of the neuronal tree, which we refer to as the neuron's skeleton, contains precise information on length, diameter, orientation and branching pattern.

2. To access exact surface and volumetric measures, we adapted the geodesic active contour algorithm (Caselles et al., 1997; Schmitt et al., 2004) to fit the idealized cylindrical shape of previously generated skeleton reconstruction to actual image data, resulting in precise boundary definition.

3. To accelerate the reconstruction process, we skeletonize threshold segmented confocal image stacks with the TEASAR algorithm (Sato et al., 2000) to generate preliminary wire models, which then serve as an initialization for the above-mentioned tracing algorithm. This fully automates the reconstruction process in cases of simple branching (for instance Purkinje neurons) and well-stained neurons, and significantly shortens the time needed to reconstruct neuronal trees with complex branching.

4. We present new methods for measuring staining density of 2nd channel image data along surface definitions or within their respective volume. This enables relative geometric analysis of, for instance, protein location in close vicinity to the surface of the dendritic tree or within the cytoplasm along the axis of neuronal projections.

### 3.4.1 Tracing neuronal structures

To trace the run of a neuron's processes in three-dimensional space from a stack of confocal image data, it was previously necessary to manually define midlines and diameters of all branches. This is extremely time-consuming and depends on personal judgment. These drawbacks can be overcome as depicted in Fig. 3.1. As an example, a small part of

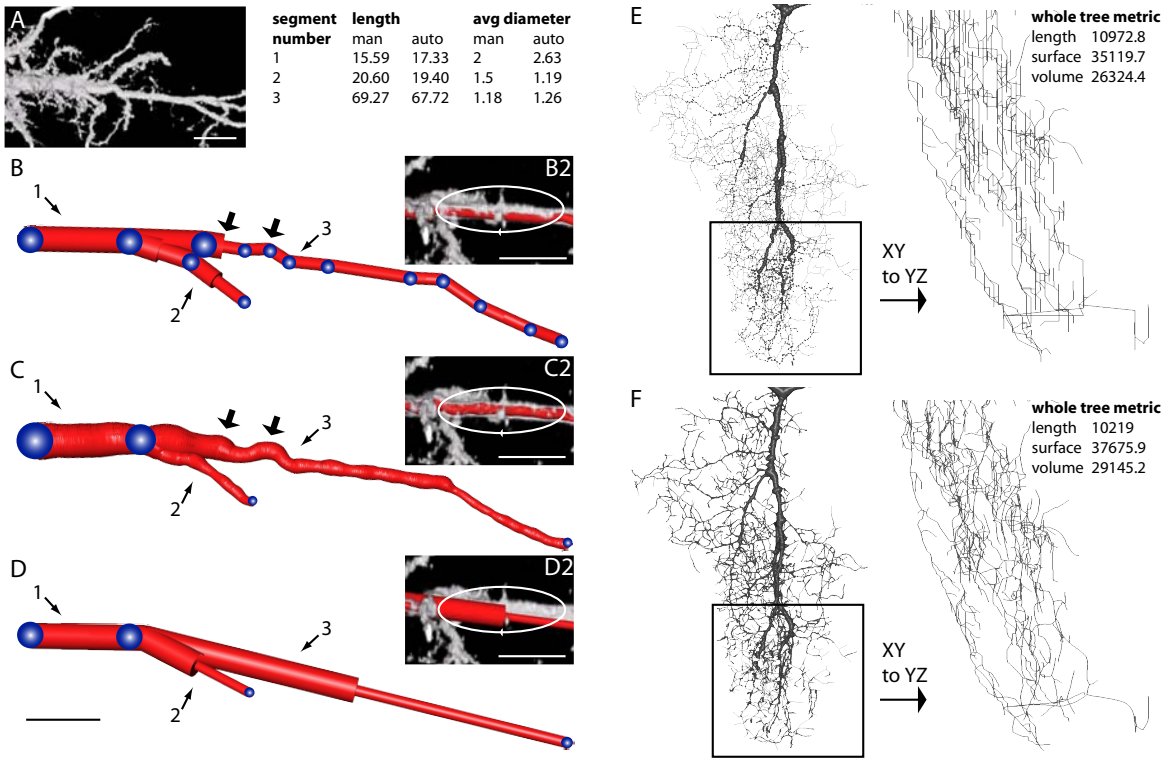


Figure 3.1: Semi-automatic midline and diameter determination beats manual mehtods. Continued on next page.

a motorneuron dendritic field (shown as a volume rendering in Fig. 3.1*A*) is reconstructed mimicking a conventional manual procedure within Amira (Fig. 3.1*B*). Typically occurring inaccuracies are obvious. First, slight bends of neuronal processes often get ignored, which leads to shortcuts in these structures (see Fig. 3.1*B2, oval*). Second, strong tapers and sharp curves are represented by unrealistic abrupt changes in diameter and sharp angular bends (Fig. 3.1*B, large arrows*). Third, image contrast must be adjusted to make small and, therefore, weakly-stained structures visible during reconstruction. The perceived diameter of all structures then will then appear thicker, thus introducing further inaccuracy. As a consequence the resulting reconstruction reflects only the coarse morphology, and an inordinate amount of time must be invested in manually describing tapers and curves with a small enough step size. Even a small step size cannot compensate for the restriction of manual reconstructions to the image plane of every optical section of confocal image data. This is expressed in a stair-like appearance of the midline's course in a y-z aspect of the reconstruction, resulting in mis-estimation of length (Figs. 3.1*B, D, E*). This problem becomes strikingly obvious in a manual reconstruction of an entire dendritic tree (Fig. 3.1*E*). To overcome these limitations we developed a semi-automatic

Figure 3.1: continued

*A*: a small part of an intracellularly labeled dendritic field is shown as volume rendering from a stack of optical section. Manual geometric reconstructions (mimicking conventional manual procedures) ao the main dendrite (*B* and *C*) are compared with geometric reconstructions of the same dendrite obtained with a new semiautomatic method (*C*). *B-D*: all points defined by user interaction are depicted in blue. Manual reconstruction requires that the user defines all center points and diameters manually and by personal judgment of the confocal image stack (blue spheres in *B*). To follow the 3-dimensional run of the dendrite, diameters must also be user-defined between branchpoints (blue spheres in *B*). Nevertheless, even with multiple user definitions for a single dendritic branch, atrificial abrupt changes in diameter and sharp bends occur (bold arrows in *B*), and slight bends often get ignored (see selective enlargement in *B2*). Applying our semi-automatic method (*C*), only branchpoints and endpoints have to be defined by the user (see blue spheres in *C*), whereas the interconnecting link segment is traced automatically with preselctable step size at single voxel resolution (*C*). This reduces time investment [compare number of user-defined blue spheres in manual (*B*) and in semi-automatic (*C*) method], and it also precisely describes sharp (bold arrows in *C*) as well as slight bends (see selective enlargement in *C2*). If the same amount of pints is user-defined (*D*) as needed for the semiautomatic procedure (*C*), the accuracy of the resulting manual reconstruction is strongly impaired. Resulting error of the manual reconstruction compared with the new semiautomatic method is depicted quantitatively in the table in *A*. To show the resulting difference for an entire dendritic tree, a manual reconstrution of the dendritic field of an insect motorneuron (*E*) and its revision with the semiautomatic method (*F*) are depicted in xz-view in *E* and *F*. Selective enlargements of the distal ends in yz-view show only the midlines. This shows that the manual reconstrions's midline is restricted to optical sections of the confocal microscope, resulting in a stair-like appearance and false estimations of dendrite lenght and branch trajectory.

reconstruction algorithm, only demanding user-provided information on interconnectivity. One method is to interactively define connected locations within the neuronal tree. The link segment is then traced automatically, producing a string of connected cylindrical compartments. Under the assumption of approximate cylindrical shape of the stained structures, the compartments' axis and radii are fitted into the confocal image stack data by iteratively optimizing their values to achieve best image data congruency. The method does not depend on boundary definition by fixed threshold levels, but calculates intensity gradients to determine boundary information (see 3.3). Branchpoints are created, choosing already-reconstructed parts as starting or endpoint. Therefore, to measure the geometry of a complete neuronal tree, only the location and connection pattern of branchpoints and endpoints must be defined manually. The algorithm automatically optimizes branchpoint location in 3 dimensions, but does not correct for user defined branchpoints located outside the original staining. Branchpoints that are left out of the calculation will

result in a straight reconstructed segment.

To show the advantages in the accuracy of this algorithm, we revised the manual reconstruction shown in Fig. 3.1*B* with our semi-automatic method. The resulting reconstruction (Fig. 3.1*C*) is a better fit to the confocal image data than the manual one, and is independent of varying staining intensities. It precisely describes slight and sharp bends as well as continuous tapers (Fig. 3.1*C large arrows, C2*), resulting in an exact geometrical reconstruction of neuronal processes. The center point of each compartment is not restricted to the image planes, but is adjusted to lie in the center point of its staining intensity distribution (see 3.3). Therefore, the dependency of length accuracy on optical section thickness is strongly diminished.

In addition to the improved accuracy, the semi-automatic reconstruction process is much faster than manual approaches, because the number of points that have to be defined is considerably reduced (Figs. 3.1*B, 1C, blue spheres*). The step size in which the skeleton's midline and diameter are determined can be adjusted to any value, limited only by the computational power of the computer, and not by the time invested by the experimenter. In contrast, when reducing the number of manually defined points to the number needed for the semi-automatic reconstruction, but not applying the new algorithm, the resulting reconstruction is greatly impaired (Fig. 3.1*D*). If the metric parameters of the manual reconstruction are compared to those of the precise semi-automatic reconstruction, for example in the case of segment 1 in Fig. 3.1*B* to *D*, the deviation of the manual reconstruction for single segments is as high as 10% in the length and 26% in its radius. The inaccuracy of the midline's course in manual reconstructions as compared to the high accuracy of the new tool presented here is further demonstrated in Fig. 3.1*E* to *F*. The x-y view of an entire dendritic tree of an insect motorneuron is shown for a manual Neurolucida reconstruction (Fig. 3.1*E*; imported into Amira, see methods), and the same reconstruction is then fitted with the method described above (Fig. 3.1*F*). Diameter precision, smoothness of fit, midline definitions, and length calculation are all far better with the new automatic tool. This becomes especially apparent when comparing selective enlargements of the tip of the dendritic field in a y-z view (Fig. 3.1*E* and *F*). The manual reconstruction shows a stair-like appearance as compared to the smooth fit with the automatic method. Comparing the metric parameters of the reconstructions of the whole dendritic trees shown in Fig. 3.1*E* and *F*, a deviation of the manual reconstruction as high as 7% in length, 7% in surface area and 11% in volume is observed. In summary, compared to manual solutions our methods save considerable amounts of time and provide higher accuracy with respect to finding the midlines and the diameters of the neuronal segments under investigation.

### 3.4.2 Boundary determination / distance map calculation / surface extraction

As the cylindrical fit discussed above precisely describes the midline of neuronal structures, it only approximates the actual run of the surface of the neuron and does not give good boundary definition for non-tubular structures. Exact surface representation of neuronal structures may be of fundamental importance, however, when exact volumetric measures are needed, and also for a proximity correlation between multiple structures acquired when considering multiple channel image data.

Most surface extraction methods rely on global threshold criteria, although confocal image stacks bear method-constrained data blurring and distortion described through the point spread function (PSF), as well as decreased fluorescence intensity with increased distance from the site of dye injection due to dye diffusion delay before sample fixation or live tissue image acquisition. The confocal image data can be corrected for the microscope and tissue specific PSF by applying deconvolution algorithms, principally enabling threshold-based image segmentation to build volume and surface reconstructions. Dye concentration gradients, however, may significantly influence accuracy particularly in distant parts of the neuron. Thin processes with fluorescent signals which are close to background noise, staining discontinuities, and ruptures occurring through histological processing need manual editing, which is subject to individual perception. To illustrate the importance of developing methods other than globally-defined threshold values for boundary extraction, we show a skeleton reconstruction of an individual dendritic growth-cone obtained with the semi-automatic method superimposed onto a single optical section (Fig. 3.2*A* and *B*). The contrast in Fig. 3.2*A* is adjusted to make thin structures visible, whereas in Fig. 3.2*B* the contrast is left untouched, to remain the same as in the original recording, which was adjusted to exploit the full working range of the photo detector while avoiding signal saturation during image acquisition. If the interior of the neuron is defined to be composed of voxels with staining intensities as occurring within small structures, the boundaries of thick structures will be overestimated. In contrast, if the threshold value is adjusted to describe the boundary of thick structures, thin structures are completely excluded. Therefore, threshold-based surface extraction cannot be applied to neurons consisting of structures with differing staining intensities, although this is a regularly-occurring phenomenon with fluorescent-labeled neurons (Fig. 3.2*A* and *B*). To solve this problem, we use the previously-fitted skeleton to extract local threshold values for each cylindrical compartment. These local threshold values are then used by an adapted active contour algorithm to fit a 3-dimensional distance map to the image data applying smoothness con-

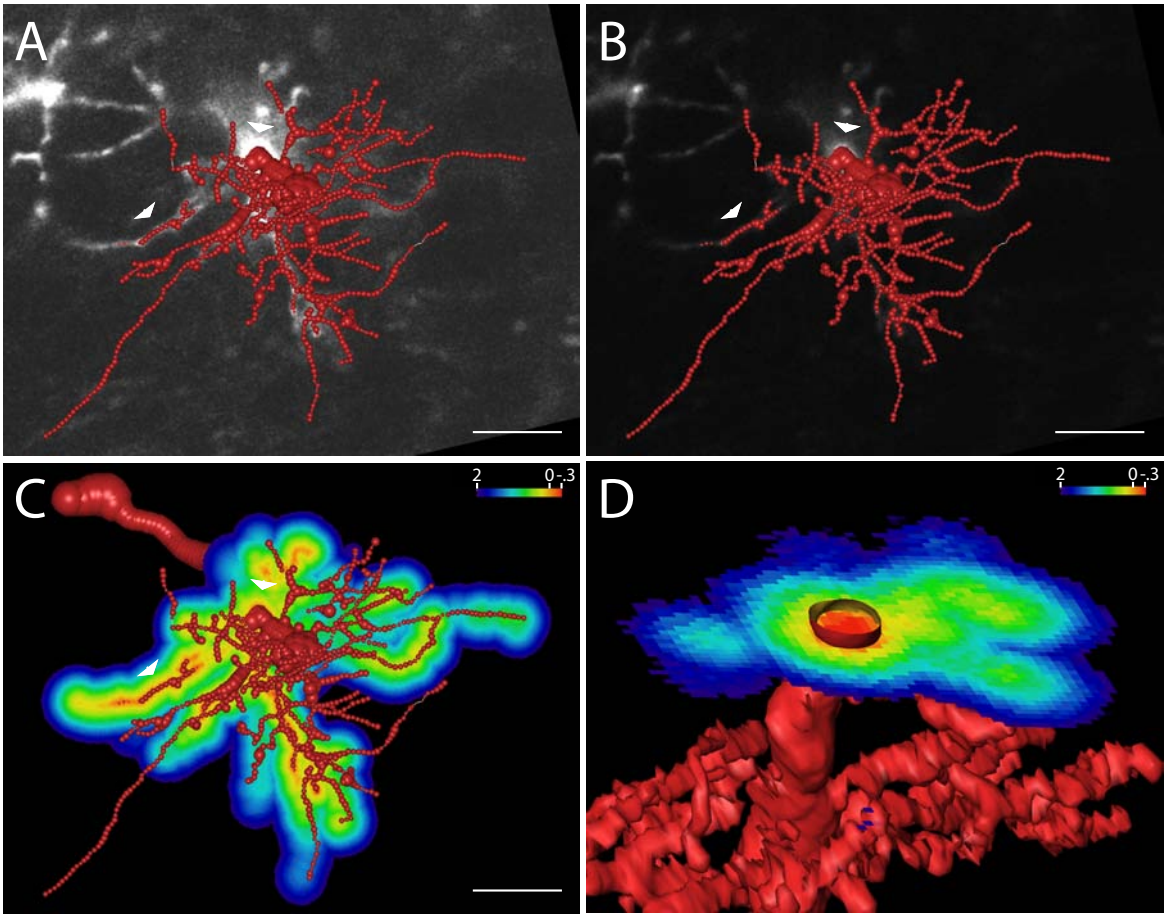


Figure 3.2: From a skeleton with fitted diameters to an exact surface. Semiautomatic cylindrical reconstruction is insensitive to lokal staining intensities, because it evaluates the steepest slope of the intensity gradient to determine the structures boundary. This problem is shown by superimposing a skeleton reconstruction onto a single optical section, in which the contrast is optimized according to 2 different criteria: 1st, to make thin neuronal processes visible ($A$), and 2nd, optimized for thicker structures ($B$). Perceived diameters depend strongly on the contrast setting as indicated by the white arrowheads in $A$ and $B$. This problem is overcome by using an algorithm to extract local thresholds. Skeleton reconstruction is used to initialize a distance map that is fitted to the actual staining distribution ($C$). Negative values mark inside of tructures, and 0 crossing indicates the structure's boundary. Arrowheads indicate sites where conventional global threshold-based boundary extraction would fail to produce correct results for either one of the neuronal processes, depending on the chosen threshold value. Resulting distance map can be converted into a binary volume definition by selecting voxels with distance values $\leq 0$ ($D$). Resulting surface overcomes limitation to strictly tubular topology and takes nontubular neuronal shapes into account ($D$), thus representing a precise surface definition.

straints (see methods). The distance map has the same voxel size as the original image data, whereby every voxel maintains the distance value to the nearest patch of neuronal

surface (Fig. 3.2*C*). Negative values mark the inside of structures; zero-crossings mark the boundary. This distance map can be threshold-segmented to obtain a binary volume definition. A precise triangulated surface reconstruction can be generated, for example, by applying the generalized marching cube algorithm (Fig. 3.2*D*).

### 3.4.3 Complete automation by skeletonization of threshold segmented image data

As described above, fixed-level threshold segmented surface reconstructions are limited in their accuracy. However, if applied to relatively large and well-stained structures, they give a good preliminary approximation of the actual neuronal shape. Here, we use the TEASAR algorithm (implementation into Amira kindly provided by Steffen Prohaska, Berlin, Germany) to extract an approximated centerline tree from prior segmented confocal image stacks, equipped with diameters. This tree is subsequently used as initialization for the previously described semi-automatic method. The interplay between both algorithms produces a skeleton, which is precisely adapted to the image data without further user interaction, not impairing the reconstruction's accuracy.

This fully automatic reconstruction approach is demonstrated for the dendritic field of a Purkinje cell, a cultured rat astrocyte and for the axonal arborization of an insect sensory neuron (wind sensitive accessory hair of *Locusta migratoria*). As the TEASAR algorithm relies on strict hierarchical organization of the segmented image data, the threshold level for all cases was adjusted to include the maximum of the arborizations while avoiding artificial formation of loops within the tree. In cells labeled as evenly as the Purkinje neuron depicted in Fig. 3.3*A* (projection view of all optical sections into one focal plane), most arborizations are included in the resulting fully automatic geometric reconstruction (Fig. 3.3*B*). This leaves the user to add only a few leftover branches with staining intensity below threshold level (arrows), or to remove a few possible loops within the threshold segmented image data. The entire reconstruction of the Purkinje cell (Fig. 3.3*A, B*) takes the experimenter less than 15 minutes working time, including the creation of dendrograms (Fig. 3.3*C*) and the extraction of accurate values for the length, diameters, and numbers of all segments and their order and orientation in 3-dimensional space.

As illustrated in Fig. 3.3 for a cultured astrocyte (Fig. 3.3*D, E*) and the central projection patterns of a locust hair receptor cell (Fig. 3.3*F*), this combination of methods fully automates the reconstruction process of many different cell types, as long as uniform staining intensity can be achieved experimentally. In the case of complex neurons with largely differing staining intensities, only clearly articulated parts of the neuronal tree

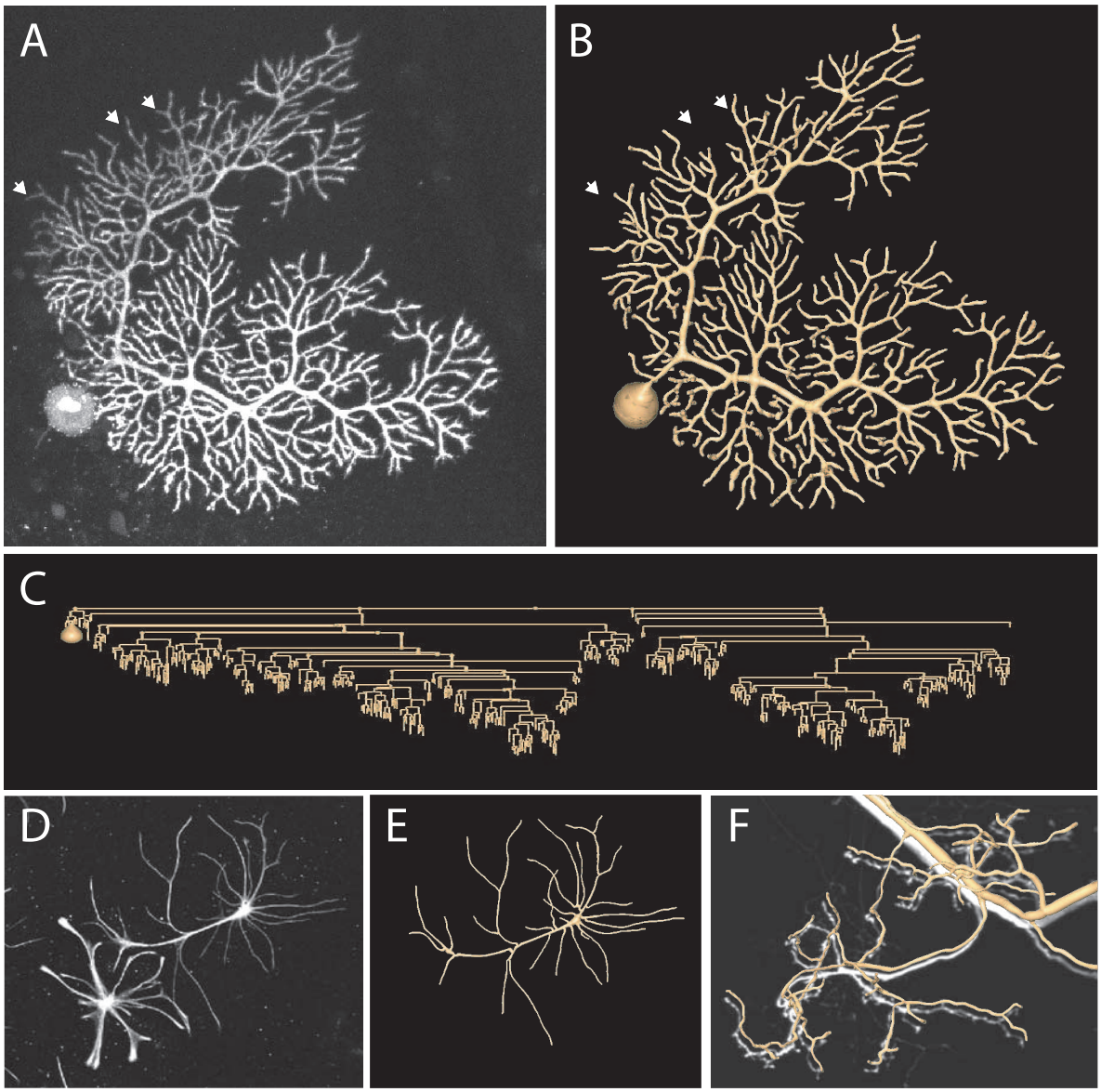


Figure 3.3: Full automatic reconstructions from confocal image stacks. Continued on next page.

can be reconstructed fully automatically (compare the high complexity of the dendritic field of the insect motorneuron in Fig. 3.4*F*). To avoid the formation of loops within the volume reconstruction, the threshold value for image segmentation then must be chosen moderately, excluding fine arborizations from the full automatic reconstruction and producing unconnected fragments of the neuronal tree as a consequence. However, this still saves the user a large amount of time, as unconnected parts can be reconnected manually and only fine structures are left over to be traced interactively applying the semi-automatic method described above (see 3.4.1).

Figure 3.3: continued

As shown for a Purkinje neuron (*A*-*C*), an astrocyte (*D* and *E*), and the central projections of a locust mechanoreceptor (*F*), fully automatic reconstructions at maximum precision are possible for well- and evenly stained neurons by combining the TEASAR centerline extraction algorithm and our adapted semiautomatic snake algorithm. This application is restricted to confocal image data that allows threshol-based volume estraction, preseving the noninterrupted and strict hierarchical organization of neuronal arboirzation. This criterion is fulfilled by image stacs of a quality as shown for a rat cerebellar Purkinje cell as a projection view in *A*. Most of the dendritic tree of this neuron was reconstructed completely automatically wihtin 15 min (*B*). Limits of fully automatic reconstruction are shown by the fact that some weakly stained projections at the upper rim of the dendritic tree ar missing (see arrows, cf. *A* and *B*). Such absent segments can be rapidly suppelemented by using our semiautomatic reconstruction procedure. The combiation of automatic and semiautomatic tools results in quite precise quantitative neural shape data with minimal time investment. Total work time from the raw data stack of the Punkinje cell shown in *A* to a dendrogram including diameters as shown in *C* was 15 min. This method is applicable for multiple cell types. *D*: projection view of a confocal image stack of cultured astrocytes. *Top right* astrocyte was selectively reconstructed (*E*) with the fully automatic tool within a few minutes. F: fully automatic reconstruction of central projections of alocust mechanoreceptor superimposed onto the projectoin view of the corresponding confocal image stack. Data courtesy of J. Brockhaus and C. Lohr (Kaiserslautern, Germany; Purkinje Neuron), D. Muench (Berlin; locust mechanoreceptor), and M. Holtje and G. Ahnert-Hilger (Berlin; astrocytes).

### 3.4.4 Evaluation of the geometric relation between multiple channel data

Neuronal function and development are strongly influenced by both, molecules that are in close spatial relationship to the dendritic surface, such as cell surface proteins, growth factors, and synaptic receptor molecules, and by molecules that occur compartmentalized in the cytoplasm, such as kinases along the neuron's projection axes. Therefore, many questions rely on an analysis of the proximity and localization relation between fluorescently-labeled structures in multiple channel image data. Ideally, the boundaries of each stained profile would be defined with a precision that allows distance measurement between surfaces in the submicron range. This is now possible for the dendritic surface by local threshold extraction, as demonstrated in Fig. 3.2. However, if this is to be done for immunocytochemically labeled molecules which are diffusely distributed throughout the neuropil, boundary definition by threshold segmentation is usually not applicable because of the antigen concentration-dependent variation of emitted light intensity.

With this in mind, we suggest a novel evaluation method for measuring the 2nd and

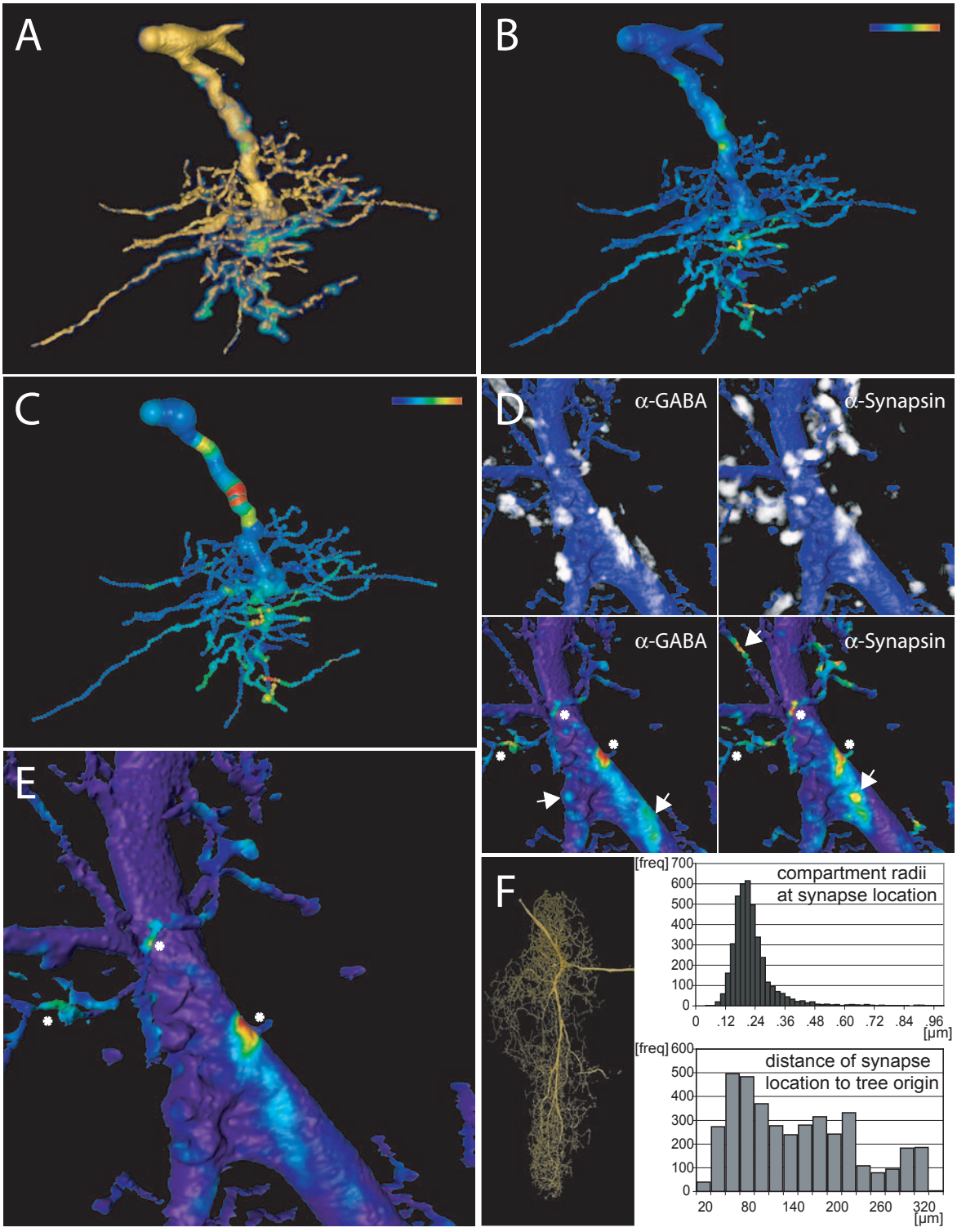


Figure 3.4: Evaluation of labeled protein concentration along dendritic surfaces at submicron resolution. Continued on next page.

3rd channel staining density around surface areas. This is done by calculating the mean staining intensity around every triangle of a triangulated surface in a user-defined dis-

Figure 3.4: continued

Analysis of the distribution of labeled putative presynaptic sites around solely postsynaptic dendritic structures (all putative synapses marked by anti-synaptotagmin, or only putative inhibitory synapses marked by anti-synaptotagmin and anti-GABA). *A*: precise surface reconstruction af a single growth-cone from an insect mononeuron (MN5 from *Manduca sexta*) as generated by local threshold fitting of the reconstructed skeleton. To neglect all labeled presynaptic proteins further than 300 nm from the growth-cone surface, a distance map around the precise surface reconstruction is used to delete all synaptotagmin label outside the 300-nm range. Resulting cut-out of the anti-synaptotagmin label is visualized as avolume redering. *B*: to visualize and quantify the average molecule concentration around each patch of the reconstructed growth-cone surface, the mean anti-synaptotagmin label staining intensity is depicted in false color code on the surface reconstruction, with warm colors representing high concentraions. For further quantification and/or export into modelling software, the surface reconstruction is projected back onto the individual cylindrical compartments of the geometric reconstruction (*C*). *D*: selective enlargement of a small part of a dendritic surface reconstruction and volume redering of both, anti-GABA immunocytochemistry from a $2^{nd}$ image channel (*top left*), and volume rendering of anti-synapsin immunostaining from a $3^{rd}$ image channel (*top right*). Average molecule concentration around each patch of the reconstructed surface is depicted for each staining (anti-GABA, *bottom left*; anti-synapsin, *bottom right*) in false color code, with warm colors representing high concentrations. Asterisks indicate sites on the dendritic surface reconstruction that are in dlose proximity to high concentrations of both immunolabels, but arrows indicate close proximity to high concentrations of 1 label only. The co-localization index [A×B/(A+B)] is shown in *E*, with warmer colors representing high concentrations of both labels within 300 nm of the surface. *F*: example of an entire dendritic tree for which this type of analysis was conducted. Numerical data for the distribution of putative GABAergic presynaptic sites detected with this method throughout the entire dendritic tree with 1,900 branch pints is plotted as a function of dendritic diameter (*top diagram*) and as a function of distance to the dendritic branch origin (see arrow).

tance in 3-dimensional space. Consequently, a neuronal surface is searched for its spatial relationship to labeled proteins by evaluating their staining intensity in a user-defined surrounding sub-volume. This staining density can then be mapped onto the surface for visualizing not only the distribution but also the staining intensity of labeled antigens along neuronal processes.

If the critical distance between both labels of the double staining is at about the same magnitude as the resolution of the recorded images, the surface has to be defined with great precision. In this case the skeleton reconstruction and consecutive surface generation described above are pivotal, particularly if synaptic proteins or surface molecules are under investigation. For instance, considering the relation of presynaptic structures to their postsynaptic membrane in the case of the Calyx of Held, the synaptic cleft is about

20 nm in size, and the vesicle pool extends to about 200-300 nm (Satzler et al., 2002) from the active zone. This sums to a distance of 220-320 nm, which would be the critical distance if vesicle-associated proteins are to be analyzed. The scanning resolution of the confocal microscope is set to 100x100x300nm, which exceeds the actual optical resolution, thus resulting in oversampling. This procedure counteracts partial volume effect and facilitates algorithmic structure recognition. However, the critical distance for evaluating staining distribution is a width of only a few voxels. To illustrate the power of this evaluation method, we chose an intracellular staining of a dendritic growth-cone of an insect motorneuron (*Manduca sexta*, MN5) combined with an antibody staining against synaptotagmin (Fig. 3.4*A* to *C*). This addresses the distribution of putative presynaptic terminals contacting the postsynaptic growth-cone.

Because of the density of immunoreactive synaptotagmin-positive profiles in the neuropil, the image information has to be excised around the dendritic surface for a better visualization of the relation between dendrites and the labeled proteins in the 2nd channel image data. This is accomplished by a distance map, generated as described above. All image intensities further than 300 nm from the dendritic surface are set to zero, so that the volume rendering of the resulting data, displayed together with the surface reconstruction, allows comprehensive visualization (Fig. 3.4*A*). To also obtain quantification, the surface reconstruction is equipped with a color code representing the staining density within 300 nm (Fig. 3.4*B*). Warmer colors represent the higher staining intensities of synaptotagmin label located within 300nm of the dendritic surface. Used in conjunction with the skeleton reconstruction of the dendrite, each patch of the surface reconstruction can be projected onto the individual cylindrical compartments. This enables analysis of geometric relation between staining distribution and the neuron's morphology (Fig. 3.4*C*). This type of evaluation makes it possible to analyze entire dendritic trees for synaptic contact probability, at least under the assumption that a high staining intensity of a synaptically-localized labeled protein might indicate a high likelihood of a putative synapse. Fig. 3.4*D* to *F* demonstrate how this type of analysis can be further extended by an additional third label. In this example a triple-staining is used to address the question of how putative GABAergic synapses might be distributed throughout an entire dendritic tree. An intracellular staining of a motorneuron is combined with immmunocytochemistry for synapsin-I (2nd channel) and for GABA (3rd channel). The motorneuron dendritic tree is reconstructed, and both immunolabels further than 300 nm from the dendritic surface are excised with the help of the distance map as described above. In Fig. 3.4*D* a small part of the reconstruction of the dendritic tree is superimposed with the remaining immunolabels for GABA (*left*) and for synapsin-I (*right*) as voltex views. In Fig. 3.4*D*

(*bottom*) the mean staining intensities of the immunolabels within 300 nm distance of the reconstructed surface are visualized on the dendritic surface in false color code. Asterisks indicate co-localization of high staining intensities of GABA and of synapsin-I on the dendritic surface and arrows indicate sites on the surface which are in close relation to a high staining intensity of one label only. Calculating the correlation between both yields a color map which results from co-localization of both, GABA and synapsin-I at high staining intensities within 300 nm of the dendritic surface (Fig. 3.4*E*). This offers a method of assessing the distribution of putative synapses of a specific transmitter throughout entire dendritic trees on the light microscopic level. As all staining intensity maps and correlation analysis can be projected onto the skeleton reconstruction, numerical data is available. As an example we analyzed the occurrence of putative GABAergic synapses detected with this method through the entire dendritic tree of an insect motorneuron (Fig 3.4*F*). The frequency of putative GABAergic synapses is plotted as a function of dendrite radius and as a function of the distance of the origin of the first order branch of the tree. As supplemental data a movie can be downloaded, showing the geometric reconstruction of the complete dendritic tree and a close-up into the subsequently generated surface reconstruction. The surface reconstruction is then embedded into the original image data of the intracellular staining, Synapsin-I label and GABA-label consecutively and equipped with the color codes generated as described above. This movie allows a comprehensive judgment on the applicability of the method. Many other numerical analyses are possible, as this is just to demonstrate the power of quantitatively evaluating proximity relations from multiple fluorescent labeled channels. In principle, the distribution of every molecule which gives a clear label in immunocytochemical detection can be analyzed. Depending on the scale, correction for chromatic aberration of the optical path may have to be applied before (Wouterlood et al., 1998).

To measure the distribution of labeled cytoplasmic molecules along neuronal arborizations, the staining intensities of labeled antigens in the interior of the cell surface must be evaluated with regard to their distribution along the neuron's projection axis. To ensure correct definition of the cell's interior, a precise definition of neuronal shape - irrespective of the idealized cylindrical shape of geometric reconstructions - is of equal importance as for surface-localized proteins. Therefore, a distance map has to be computed as described above to calculate the mean staining intensity of 2nd channel image data within the volume of all skeleton nodes. The volume corresponding to a node is first confined to lie on the node's side of the planes orthogonally intersecting the straight lines to its neighbors in their center point. Second, its voxels must hold a negative value in the distance map.

## 3.5 Discussion

We describe a novel and ready-to-use tool set which enables fast and reproducible geometric reconstruction of fluorescent-labeled neuronal arbors from confocal or two-photon image stacks. As demonstrated, the reconstruction accuracy is very high, and it is largely independent of the individual doing the reconstructing. In addition, we introduced a technique to analyze staining intensity distribution along neuronal projections with respect to their surface or cytoplasmatic localization using multiple channel image stacks. This method allows investigation of protein distribution and concentration along whole neuronal trees without time consuming immuno-electron microscopy (EM) studies. Due to limits in optical resolution, however, the method is restricted in its applicability. It has to be carefully tested for each type of analysis conducted (for example by acquiring test images of pressure injected fluorescently labeled beads) and can not replace EM studies for many questions. If co-applied with the geometric reconstruction described above, metric correlation analysis with respect to the neuronal morphology is possible. Combined with the recent achievements in two-photon imaging and genetically-expressed dyes this method will allow to estimate the relative concentration variations of molecules along the surfaces of living and growing neurons to be determined at the optical resolution the imaging setup delivers. The key of this new approach is to statistically evaluate staining intensity distribution with respect to geometry. This may be particularly useful for evaluating morphogenetic gradients, as occurring for instance from guidance molecule distribution during CNS development.

Image stacks from well- and evenly-stained neurons that are acquired at high scanning resolution without detector saturation can now be reconstructed within minutes, as demonstrated for the examples of a Purkinje cell and the afferent projections of an insect mechanoreceptor neuron. Dendritic spine necks show distinct morphological characteristics and are usually too thin for automatic recognition, and thus, must be reconstructed semi-automatically by defining their origins on the dendrite. Algorithms optimized to detect spine morphology have recently been published by other authors (Weaver et al., 2004) and may be combined with these methods.

The combination of user interaction and semi-automatic tools now allow precise reconstructions of even the most complex dendritic fields and fine dendritic filopodia, accomplished much more quickly than with conventional methods. This will be advantageous for both, single neuron analysis (life cell imaging, modelling etc.) and the creation of neuronal morphology databases (see below).

### 3.5.1 Complete automation by centerline extraction

Centerline extraction from binary volume definition is carried out with the TEASAR algorithm. This algorithm performes closest to our intuitive perception of the structure's midline. Its disadvantage, however, is the dependency on a strict hierarchical organization of the segmented image data. Deviation from hierarchical organization, for example circular connections within the segmented image data, will occur if the threshold level for image segmentation is not chosen carefully or if the distance between two structures is below optical resolution. The TEASAR algorithm unpredictably chooses one way, regardless of the size of connection. In these cases it would be favorable to achieve a centerline of all the connections and allow the user to delete those that are unwanted. In principle this is possible by applying geometric thinning algorithms. These, however, are sensitive to non-smooth surfaces, erroneously producing a high number of artificial branches. This removes the time benefit of automatic centerline extraction, as one has to manually correct each of these. Therefore, the tool set can be further improved by developing skeletonization algorithms that also work dependably on non-hierarchal data. The programming of our tool set is strictly object-oriented, therefore allowing easy integration of other algorithms for further programming development.

### 3.5.2 Applying reconstruction on time lapse images

Time-lapse image stacks of living tissues must be analyzed to quantify growth dynamics of neurons in 3-dimensional space. Slight movement of preparations and declining fluorescent signal intensities due to dye bleaching rule out comparing structures by their absolute coordinates, or by fixed-threshold level surface reconstructions. With our reconstruction framework, however, it is possible to align a copy of a reconstruction obtained from an earlier image stack to subsequently acquired data, letting the algorithm automatically adjust it to interim movement in space. Only minor additions or deletions have to be done to reflect retraction or growth of arbors. Persisting branch points can be named individually as absolute landmarks, which enables comparison of multiple subsequent skeleton reconstructions. If additional proteins are marked with a different wavelength dye, whole cell analyses of growth dynamics can be correlated to protein distribution. These new possibilities of quantitative neuronal tree analysis may open new doors for data analysis in modern *in vivo* and *in situ* imaging studies on living neurons.

### 3.5.3 Export into modelling software

Cylindrical models of neuronal projections are commonly used to simplify neuronal geometry, and, therefore, speed up computational analysis of neuronal information processing without losing the fundamental neuronal computation characteristics (Gabbiani et al., 2001; Hausser et al., 2000; Koch and Segev, 2000; Single and Borst, 1998; Stuart and Hausser, 2001). A major problem in building these cylindrical models for computational analysis is caused by parts of the neuronal tree that show a strong deviation from a cylindrical volume to surface ratio. In such a case cylindrical compartments with nicely fitted diameters produce an insufficient approximation of the neuronal geometry for computational modelling. To overcome this limitation, the automatic generation of volume reconstructions can, in turn, be used to optimize the algorithmically built cylindrical model. Each voxel of the volume reconstruction is assigned to the nearest cylinder of the geometrical reconstruction, and thus, can be used to optimize the cylinder's geometry to best reflect either the surface or volume of the reconstructed shape or any calculated intermediate. The high accuracy of the geometric reconstruction allows optimization of multi-compartment modelling, at least with regard to the geometric variables. To allow easy transition to modelling programs, we provide export filters to generate geometrically correct models for either Genesis or Neuron. For both modelling programs, their respective innate 3-D method is deployed to specify shape, orientation, and location in three dimensions. For Neuron, sections are generated for every tree segment located between 2 branch points or one branch and an end point. Every sampling point, as generated by the semi-automatic reconstruction algorithm, is used as a 3-D point in the section. The sections are connected to each other, preserving the neuron's topology. For Genesis, compartment geometry information is created at every sampling point of the geometric reconstruction by defining a point identifier, its 3-D position and diameter, and the identifier of its preceding sampling point in the neuron's tree hierarchy. Downsampling of the spatial resolution to optimize computation speed must be done elsewhere.

### 3.5.4 Neuronal model and morphology databases

Neuroanatomical databases of reconstructed neurons can help in understanding the role of morphological variations between cell types or between individual cells of the same type. Morphological alterations of neurons occur during development (Libersat and Duch, 2004; (Cline, 2001; Wong and Ghosh, 2002), during postembryonic plasticity such as learning (Muller et al., 2002; Yuste and Bonhoeffer, 2001, 2004), but also during degenerative processes, such as ageing (Uylings et al., 2000) or diseases (Arendt, 2001). Therefore, changes

in neuronal shape have multiple causes and consequences. Accordingly, the patterns of morphological changes probably follow distinct rules. Such rules cannot be inferred from the structure of single neurons, but require to sample many neurons to extract general principles. Another major question is whether neuronal morphology falls in distinct classes or follows a continuum (Monyer and Markram, 2004). Cluster analysis of neuronal shape is necessary to address this. Such problems require to pool geometric neuronal models generated by many different individuals in databases. In this regard two things are crucial: standardization of file format and a convention about the reconstruction procedure to ensure the possibility of comparison. Our method offers the possibility to standardize not only the sampling density, but gives a high user-independency in determining the center point and diameter of every compartment of the neuronal tree automatically. However, the method can not fully account for the high variability in image data quality due to differing tissue processing or imaging setups.

The usefulness of a neuron morphology database is also dependent on the availability of physiological data recorded from each neuron. As it is not possible to achieve this if each contributor must produce labor-intensive reconstruction work, a high degree of automation is pivotal. Therefore, our reconstruction framework will provide practical simplification for this approach. To permit direct integration of our reconstruction toolset into online databases for neuronal morphology, it is equipped with import and export filters for the currently used SWC file format. To speed up database buildup and common use by many scientists, it incorporates into the commercially available visualization software Amira, and the binary version of the reconstruction module will be downloadable at no cost at http://www.neurobiologie.fu-berlin.de/Evers.html. Having such a tool set available to many neuroscientists may help in tackling new aspects of functional neuroanatomy with the goal of addressing the functional interplay between dendritic morphology and dendritic computation, a functional relationship which lies at the very basis of information processing in our brains.

## Acknowledgements

We thank Johannes Brockhaus and Christian Lohr (a), Markus Holtje and Gudrun Ahnert-Hilger (b) and Daniel Münch (c) for the confocal image stacks of a Purkinje cell (a), cultured astrocytes (b) and locust sensory neurons (c). We thank Steffen Prohaska providing us with an implementation of the TEASAR algorithm in Amira.

## Grants

We gratefully acknowledge support by the Deutsche Forschungsgemeinschaft to J.F.Evers and C.Duch (SFB 515, A7), and Federal Ministry of Education and Research to M.Sibila and K. Obermayer. (0310962).

## References

Arendt, T. (2001). Alzheimer's disease as a disorder of mechanisms underlying structural brain self-organization. *Neuroscience*, 102(4):723–765.

Bucher, D., Scholz, M., Stetter, M., Obermayer, K., and Pfluger, H. J. (2000). Correction methods for three-dimensional reconstructions from confocal images: I. tissue shrinking and axial scaling. *J. Neurosci. Meth.*, 100(1-2):135–143.

Cannon, R. C., Turner, D. A., Pyapali, G. K., and Wheal, H. V. (1998). An on-line archive of reconstructed hippocampal neurons. *Journal of Neuroscience Methods*, 84(1-2):49–54.

Caselles, V., Kimmer, R., and Sapiro, G. (1997). Geodesic active contours. *Int. J. Comp. Vision*, 22:61–79.

Cline, H. T. (2001). Dendritic arbor development and synaptogenesis. *Curr. Opin. Neurobiol.*, 11(1):118–126.

de Brabander, J. M., Kramers, R. J., and Uylings, H. B. (1998). Layer-specific dendritic regression of pyramidal cells with ageing in the human prefrontal cortex. *Eur. J. Neurosci.*, 10(4):1261–1269.

Duch, C. and Mentel, T. (2004). Activity affects dendritic shape and synapse elimination during steroid controlled dendritic retraction in *Manduca sexta*. *J. Neurosci.*, 24(44):9826–9837.

Euler, T. and Denk, W. (2001). Dendritic processing. *Curr. Opin. Neurobiol.*, 11(4):415–422.

Gabbiani, F., Mo, C. H., and Laurent, G. (2001). Invariance of angular threshold computation in a wide- field looming-sensitive neuron. *J. Neurosci.*, 21(1):314–329.

Glaser, J. R. and Glaser, E. M. (1990). Neuron imaging with neurolucida - a pc-based system for image combining microscopy. *Computerized Medical Imaging and Graphics*, 14(5):307–317.

Hausser, M., Spruston, N., and Stuart, G. J. (2000). Diversity and dynamics of dendritic signaling. *Science*, 290(5492):739–744.

Kass, M. (1988). Snakes: active contour models. *J. Comp. Vision*, 1:321–331.

Koch, C. and Segev, I. (2000). The role of single neurons in information processing. *Nat. Neurosci.*, 3 Suppl:1171–1177.

Krichmar, J. L., Nasuto, S. J., Scorcioni, R., Washington, S. D., and Ascoli, G. A. (2002). Effects of dendritic morphology on ca3 pyramidal cell electrophysiology: a simulation study. *Brain Research*, 941(1-2):11–28.

Libersat, F. and Duch, C. (2004). Mechanisms of dendritic maturation. *Mol. Neurobiol.*, 29(3):303–320.

Mainen, Z. F. and Sejnowski, T. J. (1996). Influence of dendritic structure on firing pattern in model neocortical neurons. *Nature*, 382(6589):363–366.

McAllister, A. K. (2000). Cellular and molecular mechanisms of dendrite growth. *Cerebral Cortex*, 10(10):963–973.

Miller, F. D. and Kaplan, D. R. (2003). Signaling mechanisms underlying dendrite formation. *Curr. Opin. Neurobiol.*, 13(3):391–398.

Monyer, H. and Markram, H. (2004). Interneuron diversity series: Molecular and genetic tools to study gabaergic interneuron diversity and function. *Trends Neurosci.*, 27(2):90–97.

Muller, D., Nikonenko, I., Jourdain, P., and Alberi, S. (2002). Ltp, memory and structural plasticity. *Curr. Mol. Med.*, 2(7):605–611.

Rall, W., Burke, R. E., Holmes, W. R., Jack, J. J. B., Redman, S. J., and Segev, I. (1992). Matching dendritic neuron models to experimental- data. *Physiol. Rev.*, 72(4):S159–S186.

Sato, M., Bitter, I., Bender, M. A., Kaufman, A. E., and Nakajima, M. (2000). Teasar: Tree-structure extaction algorithm for accurate and robust skeletons. *Pacific Conf Comput Graph Appl 2000*, pages 281–289.

Satzler, K., Sohl, L. F., Bollmann, J. H., Borst, J. G., Frotscher, M., Sakmann, B., and Lubke, J. H. (2002). Three-dimensional reconstruction of a calyx of held and its postsynaptic principal neuron in the medial nucleus of the trapezoid body. *J. Neurosci.*, 22(24):10567–10579.

Scharff, C. (2000). Chasing fate and function of new neurons in adult brains. *Curr. Opin. Neurobiol.*, 10(6):774–783.

Schmitt, S., Evers, J. F., Duch, C., Scholz, M., and Obermayer, K. (2004). New methods for the computer-assisted 3-d reconstruction of neurons from confocal image stacks. *Neuroimage.*, 23(4):1283–1298.

Scott, E. K. and Luo, L. Q. (2001). How do dendrites take their shape? *Nature Neuroscience*, 4(4):359–365.

Segev, I. and London, M. (2000). Untangling dendrites with quantitative models. *Science*, 290(5492):744–750.

Single, S. and Borst, A. (1998). Dendritic integration and its role in computing image velocity. *Science*, 281(5384):1848–1850.

Spitzer, N. C. (2002). Activity-dependent neuronal differentiation prior to synapse formation: the functions of calcium transients. *J. Physiol Paris*, 96(1-2):73–80.

Stuart, G. J. and Hausser, M. (2001). Dendritic coincidence detection of epsds and action potentials. *Nature Neuroscience*, 4(1):63–71.

Uylings, H. B. M. and van Pelt, J. (2002). Measures for quantifying dendritic arborizations. *Network-Computation in Neural Systems*, 13(3):397–414.

Uylings, H.B.and West, M., Coleman, P., and de Brabander, J.M.and Flood, D. (2000). Neuonal and cellular changes in the aging brain. In Clark, C. and Trojanowski, J., editors, *Neurodegenerative Dementias. Clinical Features and Pathological Mechanisms*, pages 61–76. McGraw-Hill, New York.

van Pelt, J., van Ooyen, A., and Uylings, H. B. M. (2001). The need for integrating neuronal morphology databases and computational environments in exploring neuronal structure and function. *Anatomy and Embryology*, 204(4):255–265.

Weaver, C. M., Hof, P. R., Wearne, S. L., and Lindquist, W. B. (2004). Automated algorithms for multiscale morphometry of neuronal dendrites. *Neural Computation*, 16(7):1353–1383.

Wong, R. O. L. and Ghosh, A. (2002). Activity-dependent regulation of dendritic growth and patterning. *Nature Reviews Neuroscience*, 3(10):803–812.

Wong, W. T. and Wong, R. O. L. (2000). Rapid dendritic movements during synapse formation and rearrangement. *Curr. Opin. Neurobiol.*, 10(1):118–124.

Wouterlood, F. G., Van Denderen, J. C. M., Blijleven, N., Van Minnen, J., and Hartig, W. (1998). Two-laser dual-immunofluorescence confocal laser scanning microscopy using cy2- and cy5-conjugated secondary antibodies: unequivocal detection of co- localization of neuronal markers. *Brain Research Protocols*, 2(2):149–159.

Yuste, R. and Bonhoeffer, T. (2001). Morphological changes in dendritic spines associated with long-term synaptic plasticity. *Annu. Rev. Neurosci.*, 24:1071–1089.

Yuste, R. and Bonhoeffer, T. (2004). Genesis of dendritic spines: insights from ultrastructural and imaging studies. *Nat. Rev. Neurosci.*, 5(1):24–34.